

To be published in Optics Express:

Title: SNR Enhancement for Brillouin Distributed Optical Fiber Sensors Based on Asynchronous Control

Authors: Peixuan Zhang,Biwei Wang,Yanan Yang,Abul Azad,Kuo Luo,Kuanglu YU,Changyuan Yu,Chao Lu

Accepted: 05 January 22

Posted 06 January 22

DOI: <https://doi.org/10.1364/OE.447963>

© 2022 Optical Society of America under the terms of the [OSA Open Access Publishing Agreement](#)

OPTICA
PUBLISHING GROUP
Formerly OSA

1 **SNR Enhancement for Brillouin Distributed
2 Optical Fiber Sensors Based on
3 Asynchronous Control**

4 **PEIXUAN ZHANG,^{1,2,3} BIWEI WANG,⁴ YANAN YANG,^{1,2} ABUL KALAM AZAD,⁵
5 KUO LUO,^{1,2} KUANGLU YU,^{1,2,*} CHANGYUAN YU,⁴ AND CHAO LU⁴**

6 ¹*Institute of Information Science, School of Computer and Information Technology, Beijing Jiaotong
7 University, 100044, Beijing, China*

8 ²*Beijing Key Laboratory of Advanced Information Science & Network Technology, Beijing 100044,
9 China*

10 ³*Weihai Campus, Beijing Jiaotong University, Weihai 264401, China*

11 ⁴*Department of Electronic and Information Engineering, The Hong Kong Polytechnic University,
12 Kowloon, Hong Kong*

13 ⁵*Department of Electrical and Electronic Engineering, University of Dhaka, Dhaka-1000, Bangladesh*

14 * klyu@bjtu.edu.cn

15 **Abstract:** We propose the asynchronous control of anisotropic diffusion (AD) algorithm, and
16 such asynchronous anisotropic diffusion (AAD) algorithm is demonstrated experimentally to
17 reduce noise from the sensing signals obtained from Brillouin distributed optical fiber
18 sensors. The performance of the proposed AAD algorithm is analyzed in detail for different
19 experimental conditions and compared with that of block-matching and 3D filtering, two-
20 dimensional wavelet denoising, AD, and non-local means algorithms. Some key factors of the
21 proposed algorithm, such as the impact of convolution kernel size on the performance of AD
22 algorithms, the influence of low sampling point number (SPN) on the quality of Brillouin
23 frequency shift and the selection of diffusion thresholds are analyzed and discussed with
24 experimental results. The experimental results validate that the AAD algorithm can provide
25 better root-mean-square error (RMSE) and spatial resolution (SR) than the other four
26 algorithms, especially for higher signal-to-noise ratio (SNR) improvement and higher SPNs.
27 For lower SPNs, the performance of AAD is also not inferior to the RMSE performance of
28 NLM and AD. The runtime of the AAD algorithm is also quite low. Moreover, the proposed
29 algorithm offers the best SR performance as compared to other noise reduction algorithms
30 investigated in this study. Thus, the proposed AAD algorithm can be an effective candidate to
31 improve the measurement accuracy of Brillouin distributed optical fiber sensors.

32 © 2022 Optical Society of America under the terms of the [OSA Open Access Publishing Agreement](#)

33 **OCIS Codes:** (060.2370) Fiber Optics Sensors; (290.5830) Scattering, Brillouin; (120.4825) Optical time
34 domain reflectometry; (100.2980) Image enhancement.

35 **1. Introduction**

36 Brillouin distributed optical fiber sensing technology has become a hot spot in the research of
37 optical fiber sensors in recent years [1-5]. Such technology has found many applications in
38 long-distance measurements of distributed temperature and strain with good accuracy [6-10].
39 The technology is based on the principle that strain and temperature changes are linearly
40 related to Brillouin frequency shift (BFS) of the local Brillouin gain spectrum (BGS) along
41 the fiber. In order to obtain BGSs with sufficiently high signal-to-noise ratio (SNR), the
42 Brillouin distributed optical fiber sensing technology demands the sampling of sensing
43 signals multiple times and averaging of such sensing signals [11]. This process takes a long
44 time to complete the measurement of BGSs along the fiber, which is not suitable for dynamic
45 measurement [12]. Consequently, the use of suitable signal denoising algorithms to enhance

46 the SNR of the BGSs along the fiber has become one of the key issues in improving the
47 performance and broadening the applications of Brillouin distributed optical fiber sensors.

48 The BGSs along the fiber as a whole can be regarded as an image. Thus, noise reduction
49 algorithms commonly applied in image and video processing have been used recently to
50 reduce noise from the BGSs. Farahani et al. [13] applied one-dimensional wavelet transform
51 for reducing the noise of the BGSs obtained from Brillouin optical time domain analysis
52 (BOTDA) sensor. The combination of ensemble averaging and two different wavelet
53 shrinkage methods in such study can shorten the sensor's measurement time by up to 90%.
54 Soto et al. [14] claimed to use two-dimensional wavelet denoising (2D-WD) and non-local
55 means (NLM) based 2D image restoration algorithms to enhance the response of distributed
56 optical fiber sensors, and to significantly improve the SNR performance up to 20 dB without
57 the assist of additional hardware. Wu et al. [15] proposed and successfully demonstrated the
58 use of advanced block-matching and 3D filtering (BM3D) based denoising techniques for
59 BOTDA sensor to achieve high SNR improvement even in the case of small sampling point
60 number (SPN) with least degradation of measurement accuracy and experimental spatial
61 resolution. Wang et al. [16] first employed video block-matching and 3D filtering (VBM3D)
62 based denoising algorithm in a 100.8 km long-distance BOTDA sensing system with a spatial
63 resolution of 2 m, and achieved a temperature uncertainty of 0.43 °C. However, such
64 algorithm suffers from high computational complexity. Luo et al. [17] also proposed the use
65 of the classic Perona-Malik (AD algorithm in this paper) model [18], which is one of the
66 anisotropic diffusion (AD) algorithms, to reduce the noise of BGS image, and demonstrated
67 the superiority of this time efficient algorithm in preserving the experimental spatial
68 resolution. However, such traditional AD algorithm has shown relatively poor root-mean-
69 square error (RMSE) performance in BOTDA noise reduction.

70 In order to demonstrate the performance of asynchronous control (AC) algorithms, we
71 propose an algorithm that combines AC algorithm with AD algorithm as an example, which
72 is termed as asynchronous anisotropic diffusion (AAD) in this paper. The proposed algorithm
73 of AAD provides better performance through AC to improve the SNR of the BGSs, while
74 suppressing the over-smooth situation and maintaining the frequency shift edge(s).

75 The contents of this paper are divided into three parts. The ‘Algorithms’ part includes the
76 principle and the execution process of AAD. In the ‘Experiments’ part, the performances of
77 five algorithms namely 2D-WD, NLM, BM3D, AD, and AAD are compared in terms of
78 RMSE and spatial resolution (SR) with the SNR increased by 12 dB to 20 dB (step of 2 dB)
79 under the SPNs of 2 to 10 (step of 2 points). Experimental results show that under high SNR
80 improvement and high SPNs, the RMSE performance and SR of AAD are both the best
81 among the five algorithms, while under low SPNs, RMSE of AAD is better than or similar to
82 NLM and AD and the best spatial resolution is still guaranteed. In the ‘Discussion’ part, we
83 first discuss the impacts of different sizes of convolution kernels on the performance of AD
84 algorithms. We then study the effect of low SPN on the acquisition of BFS. We also find that
85 under low SNR BGS samples, the anisotropic diffusion threshold of AD algorithms shows the
86 robustness. Zaslawski et al. conducted preliminary work comparing 1-D and 2-D algorithms
87 using Gaussian filter and NLM[19], and we have further investigated their performance on
88 SR. In summary, AAD algorithm is a competitive candidate for noise reduction in Brillouin
89 and other distributed optical fiber sensing systems.

90 **2. Algorithms**

91 In this part, we first introduce the principles of anisotropic diffusion algorithm[17], Catté _PM
92 [20], and asynchronous control. Then, we illustrate AAD algorithm considering the
93 requirements for BGS images to suppress local over-smooth and to enhance edge retention.

94 **2.1 Anisotropic diffusion algorithms**

95 **2.1.1 Perona_Malik model**

96 The anisotropic diffusion (AD) methods based on partial differential equations has been
 97 applied to many applications including image denoising [21], edge detection [22], image
 98 segmentation [23], image enhancement [24] and other fields. The advantage of using AD is
 99 that it can suppress noises, while maintaining or even enhancing the edges of the image. The
 100 most classic of these is the model proposed by Perona and Malik [18]:

$$101 \quad \begin{cases} \frac{\partial I}{\partial t} = \operatorname{div} \left[g(\|\nabla I\|) \cdot \nabla I \right], \\ I(t=0) = I_0 \end{cases}, \quad (1)$$

102 where I is the input image, ∇ is the gradient operator, $g(\|\nabla I\|)$ is the diffuse function [18],
 103 which can be expressed as:

$$104 \quad g(\|\nabla I\|) = \frac{1}{1 + \left(\frac{\|\nabla I\|}{\kappa} \right)^2}, \quad (2)$$

105 where κ is the gradient threshold. In our application, Eq. (1) needs to be discretized with
 106 brightness values associated with the Brillouin gain spectrum. For this, 8-direction-neighbors
 107 discretization of Eq. (1) is employed in our case, which can be given as:

$$108 \quad I^{t+1} = I^t + \lambda \begin{bmatrix} g_N \cdot \nabla_N I + g_S \cdot \nabla_S I \\ + g_E \cdot \nabla_E I + g_W \cdot \nabla_W I \\ + g_{NW} \cdot \nabla_{NW} I + g_{NE} \cdot \nabla_{NE} I \\ + g_{SE} \cdot \nabla_{SE} I + g_{SW} \cdot \nabla_{SW} I \end{bmatrix}. \quad (3)$$

109 2.1.2 Catté_PM model

110 Aiming at the shortcomings of the PM model to strong noise and the ill-posed problem, Catté
 111 et al. proposed an improved PM model, referred to as the Catté_PM model [20], in which the
 112 gradient modulus of image is replaced by the gradient modulus after Gaussian smoothing of
 113 the original image in order to obtain the diffusion weight, due to the fact that Gaussian
 114 smoothing can effectively suppress Gaussian noise.

115 Given that additive noises, such as Gaussian white noise σ , are dominant in BGS [25], the
 116 image degradation model of BGS can be expressed as Eq.(4), where BGS_0 is the Brillouin
 117 gain spectrum without noise in ideal condition and BGS is the noisy Brillouin gain spectrum
 118 in experimental conditions.

$$119 \quad BGS = BGS_0 + \sigma. \quad (4)$$

120 The gradient modulus calculated by Gaussian smoothed image can better reflect the
 121 change of the edge of BGS_0 . Therefore, we use Catté_PM to suppress Gaussian noise in BGS.
 122 Catté_PM algorithm is expressed as

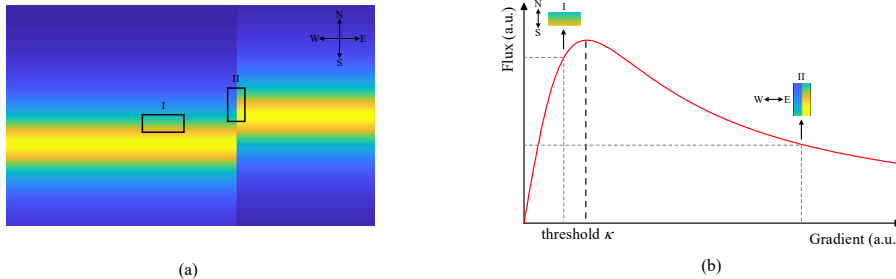
$$123 \quad \begin{cases} \frac{\partial I}{\partial t} = \operatorname{div} \left[g(\|\nabla(G_\sigma * I)\|) \cdot \nabla I \right], \\ I(t=0) = I_0 \end{cases}, \quad (5)$$

124 where G_σ is the two-dimensional Gaussian function with variance σ . In these algorithms, the
 125 flux function is used to measure the intensity of diffusion [18, 26], which can be described as:

$$126 \quad \phi = \frac{\|\nabla I\|}{g(\|\nabla I\|)}. \quad (6)$$

127 Fig. 1 shows the schematic diagram of the flux function. It can be known from Fig. 1(b)
 128 that the flat area (I) will be significantly smoothed, and the part with edges (II) will be
 129 preserved. When the noise level is equal to the diffusion threshold κ , the smoothing intensity
 130 is the largest and the noise is under the best suppression. Therefore, κ should theoretically be

131 equal to the noise standard deviation σ . However, we found in actual experiments that when κ
 132 $\geq \sigma$ with the other parameters unchanged, the noise reduction effect does not change
 133 significantly. The threshold will be further described in the discussion section.



134

135 Fig. 1. Demonstration of the schematic diagram of the flux function. (a) BGSs data with
 136 frequency shift; (b) the flux function for different areas of a BGS image.

137 2.2 Asynchronous control

138 In the study, we found that the algorithm can be iterated and after each iteration, the data that
 139 meets certain conditions are specially processed. This kind of operation will interfere with the
 140 natural evolution of data. As a result, the final result is often very different from the result
 141 obtained by allowing its natural evolution. Because the data that only meets the conditions are
 142 processed, we call it asynchronous control (AC).

143 In this study, the AC algorithm is used in ‘Local Over-smoothing Suppression’ and ‘Edge
 144 Retention’ of the AAD algorithm. And different from Catté_PM, the size of the convolution
 145 kernel for gradient calculation in AAD can be adjusted by parameters. Different convolution
 146 kernels have an impact on the runtime and noise reduction effect, which is briefly discussed
 147 later.

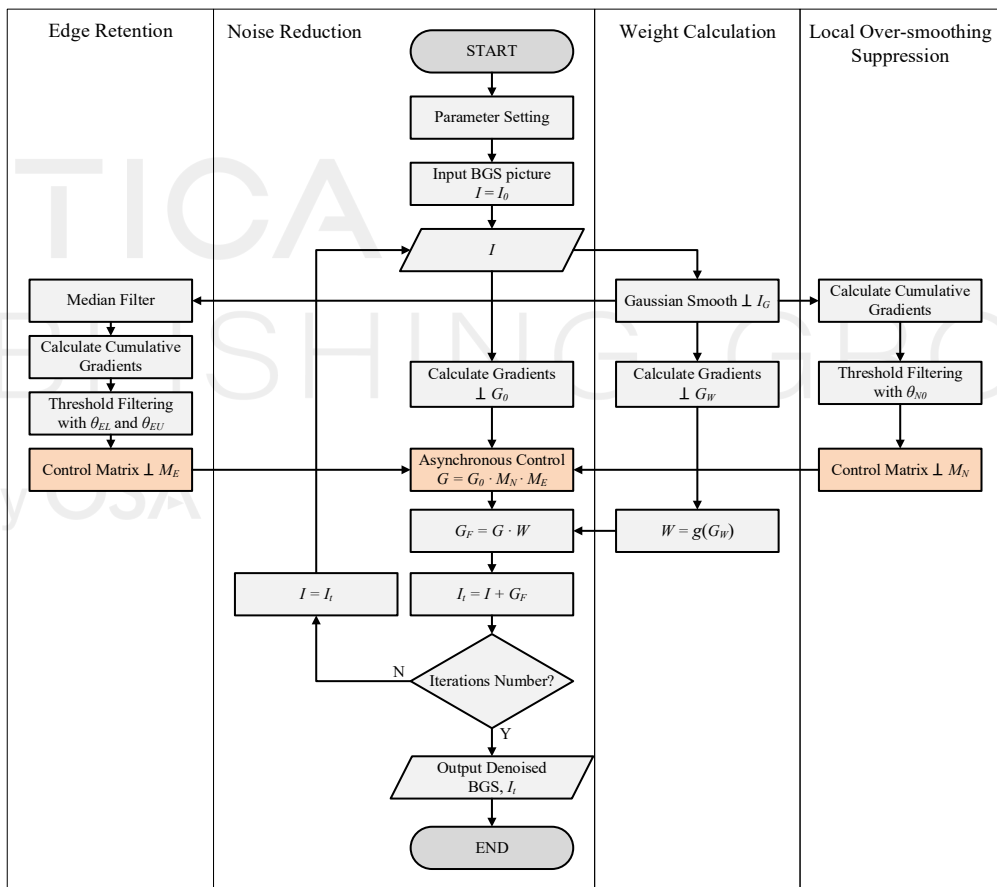
148 2.2.1 Local over-smoothing suppression

149 From Eq. (5), all points in Catté_PM algorithm participate in the calculation at each iteration.
 150 This means that the diffusion time of each point is completely consistent. From the flux
 151 function in Fig. 1(b), the smoothing intensity before threshold κ rises fast. So even if the
 152 neighboring point has small fluctuations, it will participate in the anisotropic diffusion
 153 operation to be smoothed. This will lead to over-smoothing. To suppress this, the AAD
 154 algorithm controls the diffusion of each point in each direction through the AC algorithm.

155 As shown in Fig. 2, the control method first calculates the gradient modulus absolute
 156 value of a point within a certain range, and the sum of absolute values called cumulative
 157 gradient modulus is used to represent the flatness (fluctuation) of the point in each direction.
 158 Then the accumulated gradient modulus of the entire BGS is normalized to form a normalized
 159 cumulative gradient modulus matrix in each direction in the same size of BGS image. In other
 160 words, scale its value range to between 0 and 1. The threshold θ_{N0} (in Fig. 2) is used to filter
 161 the normalized cumulative gradient modulus to find out the points whose surrounding points
 162 are relatively flat, i.e., the points of normalized cumulative gradient modulus in $[0, \theta_{N0}]$ do not
 163 participate in the anisotropic diffusion operation. This process is equivalent to a low pass
 164 filter. Finally, the control matrix M_N (a Boolean matrix, the points that in $[0, \theta_{N0}]$ is 0, the
 165 points that in $(\theta_{N0}, 1]$ is 1) is formed. Through the AC algorithm, the number of iterations to
 166 achieve the same SNR increases. However, the advantage is obvious as the overall noise level
 167 of the BGS can be uniformed, and the RMSE under the same SNR can be significantly
 168 reduced.

169 2.2.2 Edge Retention

170 Since the edge of BGS image is not a single-pixel edge, traditional edge detection algorithms
 171 such as Laplace operator [27], Sobel operator [28] are not effective in detecting BGS edges.
 172 The traditional AD algorithm cannot effectively distinguish between the edge and the noise if
 173 the sudden change of the edge gradient is submerged in the noise of BGS. Therefore, for a
 174 low SNR data, the result of diffusion may not effectively remove the noise, and it might
 175 enhance the noise. Considering the edge feature of BGS is step-like, the change of gradient
 176 before and after the edge is uniform along the frequency direction. For the case where
 177 temperature varies slowly in space, the section can be regarded as a flat area, which is
 178 processed by the local over-smooth suppression mechanism. We also use the AC algorithm in
 179 order to keep the edges. In general, the detection range of the accumulated gradient modulus
 180 of edge retention is similar to the detection range of the accumulated gradient modulus of
 181 local over-smoothing suppression. However, the range can also be set manually. In this work,
 182 by setting the lower and upper thresholds θ_{EL} and θ_{EU} in, the direction of the point where the
 183 normalized cumulative gradient modulus falls in $[\theta_{EL}, \theta_{EU}]$ does not participate in current
 184 anisotropic diffusion operation. So, it is equivalent to a band pass filter.



185
 186

Fig. 2. The flow chart of AAD algorithm.

2.3 Asynchronous anisotropic diffusion (AAD) algorithm

188 The operation of AAD algorithm is described with the help of the flowchart shown in Fig. 2.
 189 The algorithm was designed to automatically adjust the parameters based on the data to be
 190 denoised I with few manually set parameters, such as the number of iterations, the
 191 convolution kernel size, the over-smoothing threshold θ_{NO} , the edge retention thresholds θ_{EL}

192 and θ_{EU} . The Gaussian smoothing is first performed by applying median filter on BGS image
 193 to generate I_G , which is used to calculate the diffusion weight W and the cumulative gradient
 194 modulus for local over-smooth suppression. After median filtering, I_G is used to calculate the
 195 cumulative gradient modulus of edge retention. Two cumulative gradient modulus matrices
 196 are filtered by the threshold to form two control matrices M_N and M_E . At the same time, the
 197 gradient modulus G_0 is obtained through convolution with I . The step involved in AC
 198 ($M_N \cdot M_E \cdot G_0 = G$) is highlighted in the flowchart shown in Fig. 2. Then, the dot product of the
 199 gradient modulus G_F could be obtained after AC and the diffusion weight ($G \cdot W$) can be
 200 calculated. Finally, G_F is added on I to obtain the diffused image I_t for next iteration. If the
 201 number of iterations is not reached, the AAD operations (all operations above) will be
 202 performed on I_b , whilst if the number of iterations is reached, I_t will be the output. The
 203 formulae of AAD are as follows:

$$204 \quad \begin{cases} \frac{\partial I}{\partial t} = \operatorname{div} [g(\|\nabla I_G\|) \cdot \nabla I] \\ I = I_0 \\ \|\nabla I\| = 0 \end{cases} \quad t = 0, \quad (7)$$

$$\left(\{\theta_N < \theta_{N0}\} \cup \{\theta_{EL} < \theta_E < \theta_{EU}\} \right)$$

205 where t is the number of iterations, θ_N and θ_E represents the normalized cumulative gradient
 206 modulus of local over-smoothing suppression and edge retention, respectively. θ_{N0} is the over-
 207 smoothing suppression threshold, θ_{EL} and θ_{EU} are respectively the lower and upper edge
 208 retention thresholds. The result of discretization of Eq. (7) is the same as in Eq. (3). The
 209 physical meaning and optimization principles of key parameters of AAD are listed in Table 1.

210 **Table 1. The meaning and optimization principles of key parameters of AAD**

Parameter	Notation	Range	Physical meaning	Optimization principle
Number of iterations	t	$t > 0$ (integer)	The total number of algorithm iterations (\geq the actual number of iterations at each position).	Adjust it until the desired SNR improvement is obtained.
Over-smoothing suppression threshold	θ_{N0}	$0 < \theta_{N0} < 1$	For removing the part of normalized cumulative gradient modulus $< \theta_{N0}$ from diffusion operation.	Around 0.1, depends on the noise reduction effect.
Upper and lower Edge retention thresholds	θ_{EL}, θ_{EU}	$0 < \theta_{EL} < \theta_{EU} < 1$	For removing the part of $\theta_{EL} <$ normalized cumulative gradient modulus $< \theta_{EU}$ from diffusion operation.	Around 0.6 and 0.9, respectively, depends on the noise reduction effect.
Convolution kernel size	S	$S \geq 3$ (integer)	The size of the convolution kernel for anisotropic diffusion.	Typically, 3 or 5. See the discussion part.

211 **3. Experiments**

212 **3.1 Experimental setup and parameters**

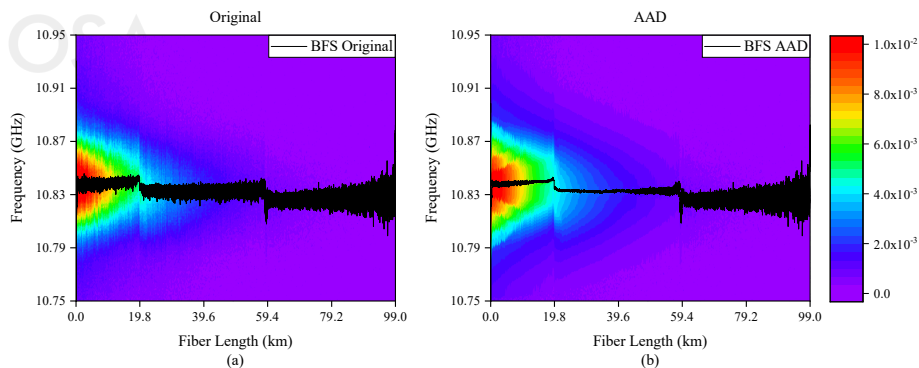
213 The setup of BOTDA system used to collect data in this experiment is the same as used by
 214 Luo et al. [17]. The total length of the optical fiber used in the setup is 99 km. In the

215 experiment, the width of pump-pulse is adopted to be 20 ns. We set the starting point at 500
 216 m from the end of the optical fiber and the BGSs along the last 500 m (i.e., 98.5 km to 99 km)
 217 have been used as raw experimental data. Because this section would be the lowest SNR part
 218 (due to attenuation and accumulated noises) which is most difficult to be processed. And the
 219 data along the first 98 km doesn't contain any hot spots or sections, while our main target was
 220 also to examine the denoising performance of various algorithms at the end of a \sim 100 km
 221 fiber.

222 The improvement of SNR and SPN are two important parameters which affect the
 223 performance of noise reduction algorithms [15]. The SPN of the experimental raw data is 10
 224 points/2-meters. We resample such raw data using piecewise linear method to generate four
 225 other SPNs of 2, 4, 6, 8 points/2-meters. Consequently, a total of 5 different SPNs are formed
 226 with the original data. The SNR of raw data is < 0 dB, and the SNR improvement varies from
 227 12 dB to 20 dB at step of 2 dB. In this work, the SNR is calculated using the method in Ref.
 228 [29]. We applied the controlled variable method to compare the noise reduction effects of
 229 different SPNs under the same SNR improvement and the noise reduction effects of different
 230 SNR improvements under the same SPN, respectively.

231 The RMSE, SR and average runtime are calculated to indicate the denoising performance
 232 of different algorithms. Here, we calculate the RMSE by comparing the actual temperature
 233 (60.3°C) of the last 192 m (from the part of the last 500 m) heating section with the measured
 234 temperature extracted by Lorentzian curve fitting (LCF) [30]. The spatial resolution is
 235 computed as the length from 10% to 90% of the rising edge [15], [31]. Lastly, the average
 236 runtime of an algorithm, which is used to quantify the algorithm's computational complexity,
 237 is calculated to be the average time taken by the algorithm from the beginning to the end of
 238 data processing under the same conditions on a same machine.

239 We use and compare the performances of different classic and most recent noise reduction
 240 algorithms in processing BGSs that includes Gaussian filtering, 2D-WD (referred to as WD in
 241 this paper), NLM, BM3D and AD algorithms. Among these algorithms, the first two have
 242 been widely used for quite a long time but the excellent performances of NLM, BM3D and
 243 AD in BGS noise reduction have been reported in recent years.

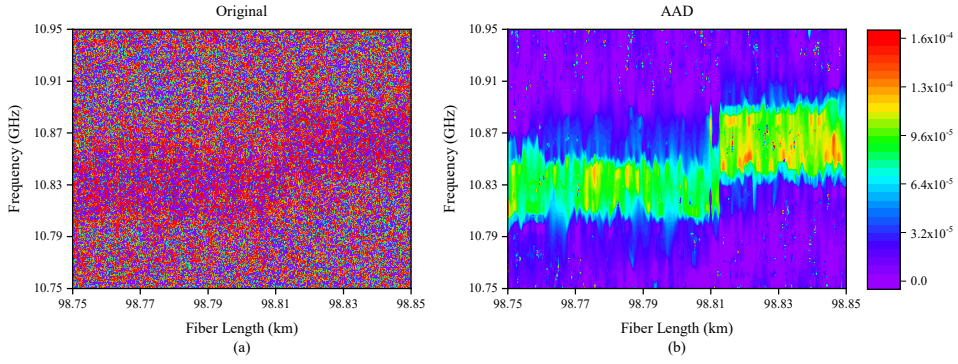


244

245 Fig. 3: Measured raw BGS (a) and the AAD denoised BGS (b) with 20 dB SNR
 246 improvement and their corresponding BFS along the FUT.

247 3.2 Experimental Results

248 In this section, we process data from two different BOTDA setups to testify the robust and the
 249 generalized performance of the AAD algorithm. Firstly, AAD is used to denoise the raw BGS
 250 data for the whole 99 km fiber, the raw BGS, denoised BGS with AAD and the BFS obtained
 251 from them are demonstrated in Fig. 3. Then, each algorithm is used to denoise the raw BGS
 252 data for the fiber section from 98.75 km to 98.85 km of the fiber. And the raw and AAD
 253 denoised BGS are demonstrated in Fig. 4.



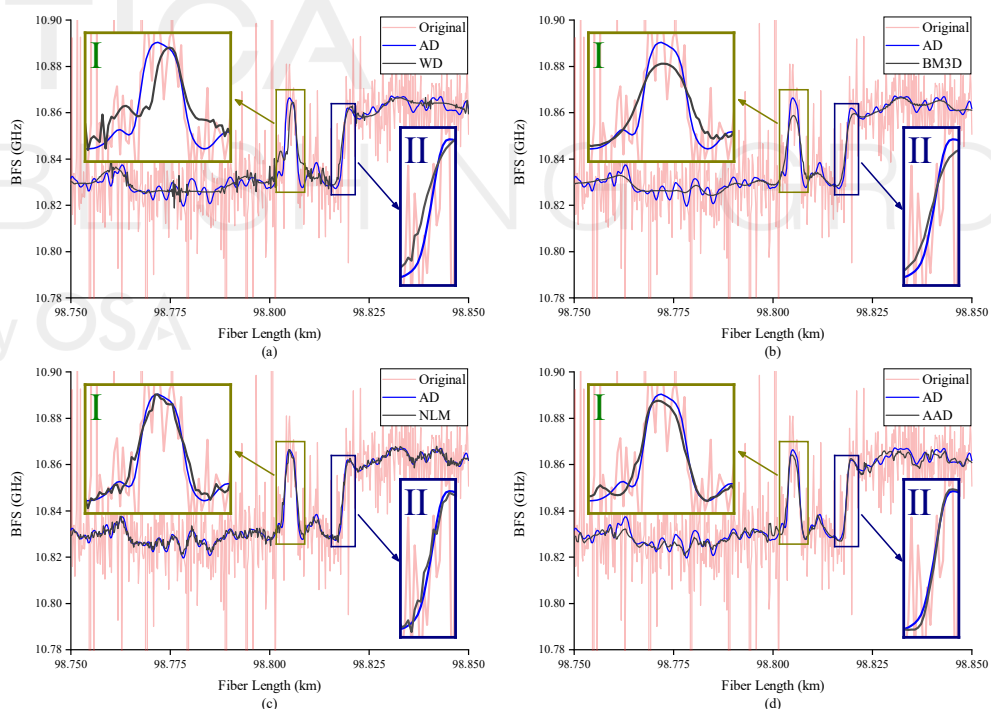
254

255
256

Fig. 4: Measured raw BGS (a) and the AAD Denoised BGS (b) with 20 dB SNR improvement from 98.75 km to 98.85 km of a 99 km section along FUT.

257
258
259
260
261

Then the noise reduction effects of each algorithm are calculated, analyzed and compared. The BFSs of the original or denoised BGSSs are determined by employing LCF. The BFSs fitted after applying noise reduction algorithms of each of WD, BM3D, NLM, and AAD are shown in Fig. 5 along with the BFS fitted without applying noise reduction algorithm as well as the BFS fitted after applying AD noise reduction algorithm.



262

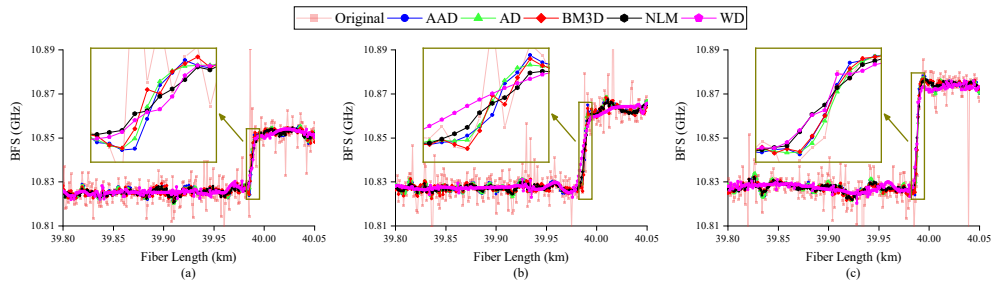
263
264
265

Fig. 5. Comparison of the origin BFS, AD denoised BFS and the BFSs after (a) WD, (b) BM3D, (c) NLM, and (d) AAD de-noising algorithms along the fiber section from 98.75 km to 98.85 km.

266
267
268
269

In the peak (I) region, the curves for using WD and BM3D are smoother than AD in Fig. 5 (a), (b). The BFS curve obtained after applying NLM noise reduction is not as smooth as that of AD, which means that the RMSE for using NLM is larger than that of AD in Fig. 5 (c). The peak of the BFS for using AAD in Fig. 5(d) at peak I is slightly lower than that of AD

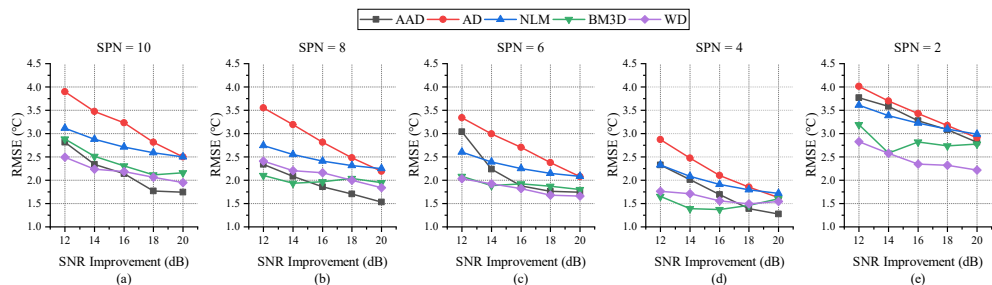
270 and NLM. However, the leading edge of its peak I rises later than the others. In the frequency
 271 shift (II) region, the lower edge of the frequency step shift for using WD and BM3D rises too
 272 early in Fig. 5(a), (b), which will make its spatial resolution far inferior to AD and make the
 273 obtained frequency shift position inaccurate. The curve for using NLM in Fig. 5(c) is similar
 274 to that of AD at peak I and the frequency shift at section II is also similar. However, this
 275 unsatisfactory BFS curve affects the spatial resolution performance and judgment of frequency
 276 shift position. At the frequency shift of AAD in Fig. 5(d), the lower edge rises lately among
 277 the four algorithms. In addition, the height of the frequency shift (II) is slightly higher than
 278 AD, which makes its spatial resolution higher than those of the other algorithms.



279

280 Fig. 6. Denoised BFSs along the section starting from 39.80 km to 40.05 km of a second 40.05
 281 km fiber after applying different noise reduction algorithms. The last 50 m section of the fiber
 282 is heated at (a) 40°C, (b) 50°C, and (c) 60°C. The inset shows the frequency shift section.

283 Secondly, another BGS data along a 40.05 km-long fiber acquired with 40 ns pump pulse
 284 is then processed, where the last 50 meters of the fiber was water-bathed at 40°C, 50°C, and
 285 60°C, respectively. The BFSs along the last 250 m are plotted in Fig. 6. The SNR of the three
 286 raw BGS images are 1.5 dB, and the SNR improvement by these five algorithms are 15 dB.
 287 As shown in the previous experiment, AAD has attained the best spatial resolution in all cases
 288 in these algorithm comparison experiments, which will be discussed later in the ‘Spatial
 289 Resolution’ section. In addition, the AAD curve has the highest rise height on the upper edge
 290 of the frequency shift in all cases. Moreover, the BFS curve obtained with AAD is relatively
 291 smooth among the five algorithms and there is no dropping in the middle of the frequency
 292 shift as in BM3D.



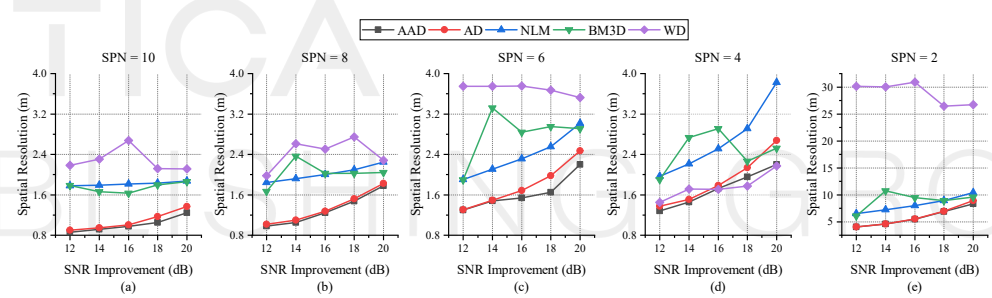
293

294 Fig. 7. RMSE of BFSs after applying AAD, AD, NLM, BM3D and WD under different SPNs.

295 3.3 Performance comparison

296 The performances of different noise reduction algorithms are compared in terms of RMSE,
 297 SR and average runtime. The RMSEs of BFSs along the 98.83 km to 98.85 km hot section
 298 after applying noise reduction algorithms are shown in Fig. 7 for five different SPNs. The
 299 results in Fig. 7 show that the RMSE performance of WD under different SPNs is not stable
 300 and the RMSEs are higher for SPNs of 4 and 8 but lower for SPNs of 2, 6 and 10. However,

301 the trend of RMSEs for using WD under the same SPN is relatively smooth. The BM3D
 302 algorithm performs almost the best among the five algorithms. However, the non-
 303 monotonicity occurs for such algorithm as can be observed easily in Fig. 7(d) and (e). The
 304 instability of these two algorithms (i.e., WD and BM3D) is caused by the resampling process
 305 used to obtain different SPNs. The NLM algorithm has a mediocre performance in RMSEs
 306 which is the most stable among these five algorithms even if the improvement of SNR is
 307 decreased. Although the trend of RMSE of AD is stable, the RMSEs are the largest for each
 308 of the five different SNR improvement used in this study. The RMSEs for using AAD under
 309 all SPNs and SNR improvements are much smaller than that of AD and the change in RMSE
 310 for using AAD increases a little if higher SPNs are used. It is also observed in Fig. 7 that the
 311 RMSEs for using AAD are comparable to that for using NLM at lower SPNs. However, the
 312 AAD outperforms NLM for higher SPNs irrespective to the SNR improvement. For instance,
 313 the RMSEs for using AAD at SPNs of 10 and 8 are significantly smaller than that for using
 314 NLM. Similarly, the RMSEs for using AAD at higher SNR improvement are also superior to
 315 that for using NLM at lower SPNs. It is further observed in Fig. 7 that the RMSE
 316 performance of AAD is slightly worse than that of BM3D, especially at lower SPNs as well
 317 as lower SNR improvement. However, at higher SPNs (8 and 10) and higher SNR
 318 improvement (> 16 dB) the performance of AAD is comparable to that of BM3D. The overall
 319 RMSE performance of AAD under a particular SPN is relatively smooth and this algorithm
 320 performs better for higher SNR improvements.



321 Fig. 8. The spatial resolution of different noise reduction algorithms.
 322

323 We then looked into the performances of different algorithms in terms of SR. The SR
 324 employing all algorithms at five different SPNs and five different SNR improvements are
 325 shown in Fig. 8. In almost all the cases, the SR performance of WD is the worst among all
 326 five while the results of NLM and BM3D are much worse than those of AD and AAD,
 327 especially for higher SPNs. The SR performances of WD and BM3D in Fig. 8 are also not
 328 stable compared to that of NLM, AD and AAD for all tested cases. As illustrated in Fig. 8 (e)
 329 that the performance of all algorithms is seriously affected by lower SPNs. The SRs for AD
 330 and AAD at all SPN and SNR improvement are very stable and almost unaffected, and they
 331 are significantly smaller than other methods. For instance, the SRs for using WD, NLM,
 332 BM3D, AD and AAD in Fig. 8(b) are 2.51 m, 2.00 m, 2.03 m, 1.27 m and 1.24 m
 333 respectively for a SPN of 8 and SNR improvement of 16 dB. Consequently, the SR
 334 performance of WD, NLM, BM3D and AD are 2.02, 1.61, 1.64 and 1.02 times worse than
 335 that of AAD. These ratios also increase if higher SPNs are applied. It is worth mentioning that
 336 the selected lengths of SRs presented here are slightly shorter than 10%-90% of the rising
 337 edge as a result of keeping the length of the straight-line fitting under different SPNs
 338 consistent. However, such results can well demonstrate the trend of SR with different SPN.

339 In addition, we also computed SRs at different temperatures for denoised BFSs shown in
 340 Fig. 6, where the SPN is 4 and SNR improvement is 15 dB. The results are shown in Table 2.
 341 The large spatial resolution at 50°C is due to the slight deviation of the rising edge position of
 342 the frequency shift from the other two temperatures. As shown in Table 2, the SR of AAD is

343 not affected by the temperature difference both before and after the frequency shift as that of
344 other algorithms. These results again confirm that the SR performance of AAD is better.

345 **Table 2. Spatial resolution (SR) of different noise reduction algorithms for the 40.05 km fiber**

SR (m)	Algorithms				
	AAD	AD	BM3D	NLM	WD
Temp (°C)	40	2.23	2.49	4.02	8.03
	50	3.25	4.14	7.66	8.64
	60	2.71	2.84	3.08	5.24
					3.82

346 Next, we investigate the complexity of these algorithms in terms of the data processing
347 time. To achieve this, the runtimes of each algorithm at all SPNs are recorded and then
348 averaged at different SNR improvements with the parameters listed in Table 4. The hardware
349 platform for implementing different noise reduction algorithms is composed of an Intel®
350 Core i7-7700HQ CPU @ 2.80 GHz and a 16 GB RAM, and the Python interpreter is Python
351 3.7. The runtimes for using five different algorithms are presented in Table 4. The results
352 show a longer runtime for a larger SPN for all algorithms, i.e., larger sample numbers of the
353 BOTDA traces. For all five different SPNs, BM3D takes the longest runtime to obtain the
354 results. In descending order, the average time consumption are then followed by AAD, WD,
355 NLM, and AD, where AD takes the shortest runtime. The runtime of AAD is reasonably good
356 as compared to other algorithms, especially for lower SPNs, and it requires only 3% to 24%
357 of that of BM3D and takes slightly longer than other algorithms.

358 **Table 3. Values of parameters used in the denoising algorithms**

Algorithms	Parameters	Setting
AAD	Diffusion constant	1/8
	Diffusion equation	Eq. (7)
	Kernel size	5×5
BM3D	Sliding step	2
	Block size	12×12
	Search window size	13×13
	Max matched blocks	16
	Threshold strategy	Hard & Wiener
NLM	Similarity window size	3×3
	Search window size	13×13
AD	Diffusion constant	1/8
	Diffusion equation	Eq. (1)
WD	Wavelet	Sym5
	Decomposition level	5
	Threshold strategy	Hard

359 We would like to point out that the runtime of AD algorithm is proportional to the
360 iteration number needed to process the data. So, if we consider only that number, the time
361 taken by AAD should be 2 to 4 times longer than that by AD. However, AAD suppresses
362 over-smooth points and edge points from participating in the smoothing process, which
363 results in a smaller SNR increase for each iteration than AD. Hence, it requires more iteration
364 to obtain the same SNR improvement as the latter. In addition, AAD also performs AC
365 operation at each iteration, and this additional calculation also prolongs the time consumption.

Table 4. Runtime for applying different noise reduction algorithms

Runtime (s)	SPNs					
	2	4	6	8	10	
Algorithms	AAD	0.85	4.45	16.66	30.30	40.60
	BM3D	31.31	64.10	98.73	132.24	165.66
	NLM	0.30	0.86	1.58	2.09	2.57
	AD	0.037	0.08	0.38	0.57	0.58
	WD	1.16	2.23	3.28	4.63	5.81

4. Discussion

In this part, we will further discuss some important issues in the experiment, which includes the impact of the convolution kernel size on algorithm performance, the impact of a low SPN on BFS, the robustness of anisotropic diffusion threshold, and the performance comparison of 1D and 2D algorithms on noise reduction.

4.1 Convolution Kernel Size

In our study, the size of the convolution kernel has a large impact on AAD. The kernels, which have eight different directions as shown in Fig. 9, can be a square with an odd size greater than or equal to 3 as long, i.e., 3×3 , or 7×7 .

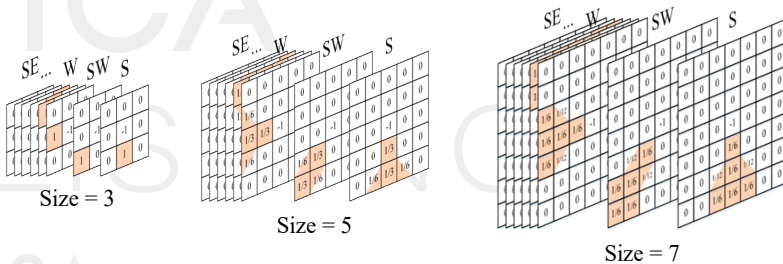


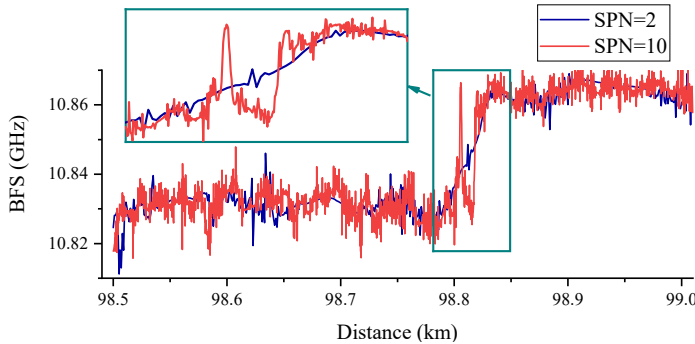
Fig. 9. Convolution Kernels of Different Sizes.

In AD algorithms, which include both AD and AAD, the convolution kernel determines the degree of data relevance at each iteration. In terms of RMSE, a larger kernel has a wider convolution range with more neighboring points when smoothing, and a wider convolution range will improve the RMSE performance. However, when it comes to spatial resolution, a wider convolution range will cause a decrease. As a compromise, a 5×5 convolution kernel was applied in paper. On the other hand, a larger kernel achieves the same SNR improvement employing a smaller number of iterations as compared to a smaller kernel, which can save runtime.

4.2 RMSE and SR Relationship with SPN

The overall trend of RMSE for different SPNs in Fig. 7 manifests that the RMSE drops if SPN decreases except for very low SPN (e.g., 2). The reason is that fewer sampling points along the same length on the optical fiber for RMSE are engaged in RMSE calculation. In such case, the corresponding RMSE is likely to become smaller for lower SPN. However, when $SPN = 2$ (the lowest SPN used in this study), there is a counter-trend situation and the RMSE increases significantly. This is because all of the BM3D, NLM, AD, and AAD algorithms rely on the neighboring points to judge and reduce the noise of the center point (by matching or convolution). It is assumed that any point in the matrix (BGS image) has continuity with all of or part of its neighboring points (such as edge points). However, too few

396 SPNs may undermine this continuity and cause the deterioration of RMSE. A similar situation
 397 also appears in the SR performance.



398

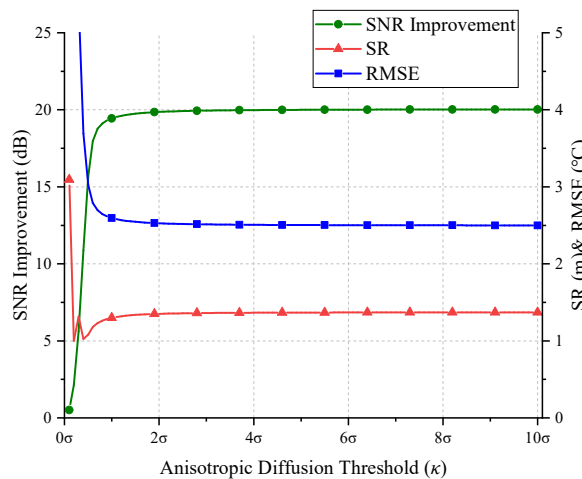
399 Fig. 10. Denoised BFSs for using WD with 12 dB SNR Improvement at SPNs of 2 and 10.

400 As shown in Fig. 8, the SR increases slowly if SPN is dropped from 10 to 4. However, the
 401 SRs of all algorithms increase abruptly at SPN of 2. This is because when the SPN is too
 402 small (e.g., ≤ 2 data points on the system's spatial resolution length, which is 2 m for the
 403 99 km system), the BGS information is greatly lost, leading to a sharp deterioration in the spatial
 404 resolution. The abrupt degradation of SR at a low SPN (SPN = 2) is illustrated in Fig. 10 as
 405 an example by using WD as this algorithm can obtain the most obvious outcome of denoising
 406 a BGS image in lower SPNs. In the BFS curve, since the 2.3 m peak section is quite close to
 407 the frequency shift section (only 11.8 m), it becomes over-smoothed and flattened to one
 408 single ramp after filtering. Therefore, low SPNs should be avoided in denoising BGSs as it is
 409 likely to cause severe SR deterioration.

410

4.3 Robustness of Diffusion Threshold

411 As mentioned in section 2.1, the noise level equal to the diffusion threshold κ would result in
 412 the largest smoothing effect. In other words, the noise is under maximum suppression.
 413 Generally, the theoretical value of the threshold κ should be equal to the noise standard
 414 deviation σ , which is confirmed by the flux function visualized in Fig. 1. However, it is found
 415 in our study that for $\kappa \geq \sigma$ with other parameters fixed, the noise reduction effect does not
 416 change significantly. In particular, for $\kappa \geq 3\sigma$, the setting of κ has almost no influence on the
 417 noise reduction effect.



418

419

Fig. 11. The SNR Improvement, RMSE and SR using AD with SPN of 10 and iterations of 22.

420 To study the effect of diffusion threshold κ , the SNR improvement, RMSE, and SR with κ
 421 are illustrated in Fig. 11, where SPN is 10 and the iteration number is 22. The AD algorithm
 422 is used as an example as it has fewer parameters which prevent other parameters from
 423 interfering with the κ robustness result. The results obtained for using AAD would be
 424 expected to be similar. As in Fig. 11, that the SNR improvement increases rapidly for slight
 425 increase of κ in the beginning until κ reaches to σ , and such SNR improvement tends to be
 426 stabilized for $\kappa \geq 3\sigma$. In addition, the RMSE drops rapidly for the increase of κ values within
 427 the range from 0.02σ to σ and becomes stabilized for $\kappa \geq 3\sigma$. It is also shown in Fig. 11 that
 428 the spatial resolution varies in a different way which fluctuates a bit until $\kappa = \sigma$ and stabilizes
 429 for $\kappa \geq 3\sigma$.

430 In fact, the diffusion threshold is designed to distinguish edges from noise. However, the
 431 gradient modulus of noise of our experimental data ($\text{SNR} < 0$) has not only the components
 432 whose amplitudes are larger than the edge but also those with smaller amplitudes than the
 433 edge. So, the edges cannot be distinguished from the noise with only one diffusion threshold.
 434 Hence, without considering the edge, the threshold κ should be set so that all the noises fall to
 435 the left side of the peak of the flux function to perform best noise reduction which can smooth
 436 the points with larger gradients. This means that the use of larger threshold κ performs better
 437 noise reduction. Considering different characteristics for edge and noise, the former has
 438 spatial continuity in BGS while the latter is mostly scattered on BGS. The combination of the
 439 feature of diffusion with AD algorithms helps to check the continuity between a point and its
 440 neighbors. Even under the same diffusion threshold, the retention effect is much stronger for
 441 the edge than for the noise. In conclusion, in order to be robust, $\kappa = 3\sigma$ is suitable for the AD
 442 algorithm family, especially for BGS data having strong noises.

443 *4.4 Performance of 1D and 2D noise reduction algorithms*

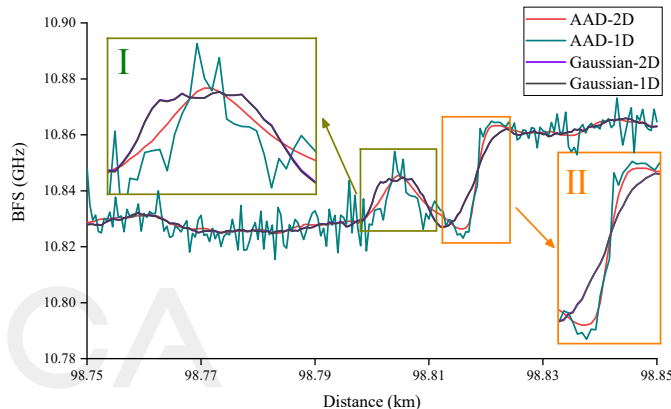
444 The performances of 1D and 2D Gaussian noise reduction algorithms with that of the AAD
 445 algorithm are also analyzed and compared. For simplicity, the spatial resolution of NLM, WD
 446 and other algorithms are not repeated here. Zaslawski et al. has carried out preliminary
 447 theoretical and experimental research on noise reduction performance of the 1D and 2D
 448 algorithms [19]. But the work does not include the influence of noise reduction algorithms on
 449 the sensor's spatial resolution, which is, however, greatly affected by the noise reduction
 450 algorithm. Hence, we analyze and compare the effect of 1D and 2D Gaussian and AAD
 451 algorithms on SR, full width at half-maximum (FWHM) of the hot spot peak (thus in meter),
 452 height of the peak (Fig. 12 inset I), and RMSE. The parameters used in 1D and 2D Gaussian
 453 approaches are the same as in Ref. [19]. For the AADs, we set the SNR improvement
 454 consistent with the 2D Gaussian noise reduction algorithm (about 20 dB). The SPN of BGS
 455 image is set to be 4, to match that in Ref. [19]. The results are listed in Table 5.

456 **Table 5. SR, FWHM, peak height and RMSE for using different algorithms**

Parameters	Algorithm			
	2D-AAD	1D-AAD	2D-Gaussian	1D-Gaussian
SR (m)	2.2	1.58	4.30	4.27
Peak FWHM (m)	7.5	2.25	9	9
Peak Frequency (GHz)	10.8454	10.8540	10.8447	10.8447
RMSE (°C)	1.28	3.02	1.44	1.49

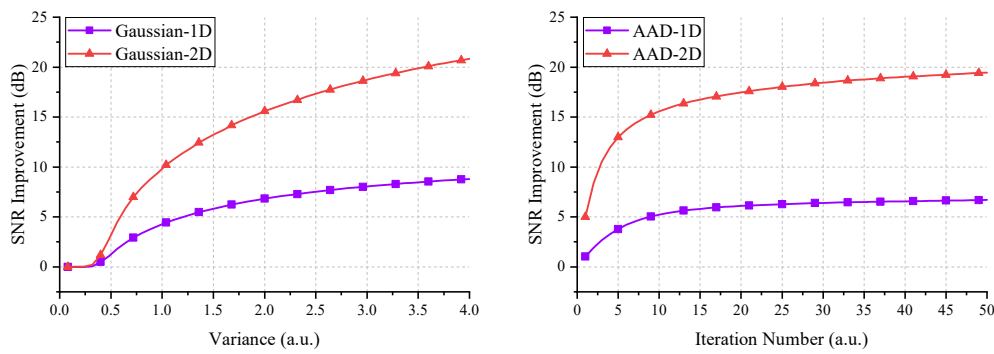
457 The 2D-AAD performs better than both Gaussian algorithms in determining all the four
 458 parameters. In particular, the widths of the peak after applying 1D and 2D Gaussian
 459 algorithms are much larger than that of 2D-AAD, indicating that it has suffered greater
 460 distortion. The SNR improvement of the two algorithms in the 2D form is 20 dB, and then the
 461 algorithms are transformed into a 1D form without changing other parameters. The results are

462 shown in Fig. 12. The BFS curves of the Gaussian methods basically overlap with each other.
 463 These results confirm the claim that the noise reduction effects of 1D (along fast axis) and 2D
 464 Gaussian noise reduction algorithms are basically the same as stated in Ref. [19]. However,
 465 this is not true for AAD. Although the SR, FWHM and peak height of 1D-AAD in Table 5
 466 appear to be better than that of 2D-AAD, its RMSE lags far behind. This is due to the poor
 467 noise reduction effect of 1D-AAD, which makes peak I and frequency shift in inset II in Fig.
 468 12 more affected by noise. This effect is also responsible for providing the inaccurate results
 469 for SR, FWHM and peak height. Although Lorentzian curve fitting has a certain overlap with
 470 the effect of 2D denoising, for AAD which operates in a non-linear way, its 2D form still has
 471 a better performance than the 1D counterpart with the same parameters.



472
 473 Fig. 12. BFSs obtained by 1D and 2D AAD, and by 1D and 2D Gaussian Filter denoising.

474 Finally, we compare the SNR improvement capabilities of 1D and 2D Gaussian filtering
 475 algorithms with that of AAD as shown in Fig. 13. Only the dimension of the algorithm and
 476 the parameters that control SNR improvement (the variance for Gaussian filter, and the
 477 number of iterations for AAD) are changed. The SNR improvements offered by the 1D
 478 algorithms are approximately 1/3 of that by the 2D counterparts. This is due to the fact that
 479 the 2D Gaussian filtering requires only a small variance to achieve the same SNR
 480 improvement as compared to the 1D Gaussian filter. And 2D-AAD needs a small number of
 481 iterations to achieve the same SNR improvement as compared to 1D-AAD. A smaller
 482 variance or a smaller number of iterations is more beneficial for maintaining spatial resolution
 483 performance, which is another reason why 2D methods should be recommended.



484
 485 Fig. 13. SNR improvement of BGS for using Gaussian Filters and AADs.

486 **5. Conclusions**

487 In this paper, we have proposed a noise reduction algorithm based on asynchronous control
488 (AC) of anisotropic diffusion (AD), and the proposed asynchronous anisotropic diffusion
489 (AAD) algorithm is applied to improve the SNR of the BGS images of the Brillouin
490 distributed optical fiber sensors. The performances of the proposed AAD algorithm have been
491 analyzed theoretically and validated experimentally in detail for various experimental
492 conditions. The experimental results show that AAD algorithm improves the RMSE
493 performance of Brillouin distributed sensors significantly as compared to AD. The RMSE of
494 the AAD is also comparable to other noise reduction algorithms (e.g., WD, NLM and BM3D)
495 currently used in optical fiber sensing technology. Moreover, the proposed algorithm has a
496 distinguished ability to maintain the spatial resolution of the fiber sensors better than AD,
497 WD, NLM and BM3D algorithms.

498 We have also discussed some critical issues in denoising sensing signals obtained from
499 Brillouin sensors. Firstly, the effect of noise reduction using 1D and 2D algorithms on the
500 spatial resolution deterioration has been investigated and analyzed in detail, which shows that
501 the 2D denoising algorithm performs better than 1D algorithm in terms of spatial resolution,
502 SNR improvement and processing speed. Secondly, we also found that the use of very low
503 SPN in BGS raw data seriously affects the SR after applying denoising algorithms, which
504 suggests the DAQ's sample rate should be larger than certain values. Finally, although the
505 diffusion threshold κ of the AD algorithm was supposed to be equal to the noise standard
506 deviation σ , our robust analysis indicates that κ should be around 3σ especially when dealing
507 with the BGSs with low SNR.

508 In summary, the proposed AAD method shows its advantages in terms of SR and RMSE
509 performance, robustness, and controllable effects in BGS image denoising. The proposed
510 asynchronous control method could also be possibly extended and combined with all cellular
511 automata algorithms to find much wider applications. The use of AC algorithms with AD
512 could be competitive in denoising sensing signals obtained from Brillouin as well as other
513 distributed optical fiber sensors to provide highly accurate distributed measurements with a
514 well-preserved spatial resolution.

516 **Funding.** This work was supported in part by the Fundamental Research Funds for the Central Universities under
517 Grant 2020JBM024, in part by the National Natural Science Foundation of China (NSFC) under Grant 61805008,
518 and in part Outstanding Chinese and Foreign Youth Exchange Program of China Association of Science and
519 Technology.

520 **Acknowledgments.** The authors would like to thank Prof. Honghong Zhou of Beijing Jiaotong University for
521 revising the language of this paper.

522 **Data availability.** Data underlying the results presented in this paper are not publicly available at this time but
523 may be obtained from the authors upon reasonable request.

525 **References**

1. A. Minardo, R. Bernini, and L. Zeni, "A simple technique for reducing pump depletion in long-range distributed Brillouin fiber sensors," *IEEE Sens. J.*, **9**(6), 633-634 (2009).
2. A. Motil, A. Bergman, and M. Tur, "State of the art of Brillouin fiber-optic distributed sensing," *Opt. Laser Technol.*, **78**, 81-103 (2016).
3. F. Bastianini, F. Matta, A. Rizzo, N. Galati, and A. Nanni, "Overview of recent bridge monitoring applications using distributed Brillouin fiber optic sensors," *J. Nondestruct. Test.*, **12**(9), 269-276 (2007).
4. F. Rodríguez-Barrios, S. Martín-López, A. Carrasco-Sanz, P. Corredora, J. D. Ania-Castañón, L. Thévenaz, and M. González-Herráez, "Distributed Brillouin fiber sensor assisted by first-order Raman amplification," *J. Lightwave Technol.*, **28**(15), 2162-2172 (2010).
5. X. Gao, Z. Yang, S. Wang, X. Hong, X. Sun, M. A. Soto, J. Wu, and L. Thevenaz, "Impact of optical noises on unipolar-coded Brillouin optical time-domain analyzers," *Opt. Express*, **29**(14), 22146-22158 (2021).
6. H. Murayama, K. Kageyama, H. Naruse, A. Shimada, and K. Uzawa, "Application of fiber-optic distributed sensors to health monitoring for full-scale composite structures," *J. Intel. Mat. Syst. Str.*, **14**(1), 3-13 (2003).

- 539
- 540
- 541
- 542
- 543
- 544
- 545
- 546
- 547
- 548
- 549
- 550
- 551
- 552
- 553
- 554
- 555
- 556
- 557
- 558
- 559
- 560
- 561
- 562
- 563
- 564
- 565
- 566
- 567
- 568
- 569
- 570
- 571
- 572
- 573
- 574
- 575
- 576
- 577
- 578
- 579
- 580
- 581
- 582
- 583
- 584
- 585
- 586
- 587
- 588
- 589
- 590
- 591
- 592
7. A. Minardo, R. Bernini, L. Amato, and L. Zeni, "Bridge monitoring using Brillouin fiber-optic sensors," *IEEE Sens. J.*, **12**(1), 145-150 (2011).
 8. C. A. Galindez-Jamioy and J. M. Lopez-Higuera, "Brillouin distributed fiber sensors: an overview and applications," *J. Sensors.*, **2012**, (2012).
 9. S. Uchida, E. Levenberg, and A. Klar, "On-specimen strain measurement with fiber optic distributed sensing," *Measurement*, **60**, 104-113 (2015).
 10. T. Horiguchi, K. Shimizu, T. Kurashima, M. Tateda, and Y. Koyamada, "Development of a distributed sensing technique using Brillouin scattering," *J. Lightwave Technol.*, **13**(7), 1296-1302 (1995).
 11. Y. Xiang, M. R. Foreman, and P. Török, "SNR enhancement in brillouin microspectroscopy using spectrum reconstruction," *Biomed. Opt. Express*, **11**(2), 1020-1031 (2020).
 12. R. Bernini, A. Minardo, and L. Zeni, "Dynamic strain measurement in optical fibers by stimulated Brillouin scattering," *Opt. Lett.*, **34**(17), 2613-2615 (2009).
 13. M. A. Farahani, M. T. Wylie, E. Castillo-Guerra, and B. G. Colpitts, "Reduction in the number of averages required in BOTDA sensors using wavelet denoising techniques," *J. Lightwave Technol.*, **30**(8), 1134-1142 (2011).
 14. M. A. Soto, J. A. Ramirez, and L. Thevenaz, "Intensifying the response of distributed optical fibre sensors using 2D and 3D image restoration," *Nat. Commun.*, **7**(1), 1-11 (2016).
 15. H. Wu, L. Wang, Z. Zhao, N. Guo, C. Shu, and C. Lu, "Brillouin optical time domain analyzer sensors assisted by advanced image denoising techniques," *Opt. Express*, **26**(5), 5126-5139 (2018).
 16. B. Wang, L. Wang, C. Yu, and C. Lu, "Long-distance BOTDA sensing systems using video-BM3D denoising for both static and slowly varying environment," *Opt. Express*, **27**(25), 36100-36113 (2019).
 17. K. Luo, B. Wang, N. Guo, K. Yu, C. Yu, and C. Lu, "Enhancing SNR by Anisotropic Diffusion for Brillouin Distributed Optical Fiber Sensors," *J. Lightwave Technol.*, **38**(20), 5844-5852 (2020).
 18. P. Perona and J. Malik, "Scale-space and edge detection using anisotropic diffusion," *IEEE T. Pattern Anal.*, **12**(7), 629-639 (1990).
 19. S. Zaslawski, Z. Yang, and L. Thévenaz, "On the 2D post-processing of Brillouin optical time-domain analysis," *J. Lightwave Technol.*, **38**(14), 3723-3736 (2020).
 20. F. Catté, P.-L. Lions, J.-M. Morel, and T. Coll, "Image selective smoothing and edge detection by nonlinear diffusion," *SIAM J. Numer. Anal.*, **29**(1), 182-193 (1992).
 21. Y. Yu and S. T. Acton, "Speckle reducing anisotropic diffusion," *IEEE T. Image Process.*, **11**(11), 1260-1270 (2002).
 22. C. Lopez-Molina, M. Galar, H. Bustince, and B. De Baets, "On the impact of anisotropic diffusion on edge detection," *Pattern Recogn.*, **47**(1), 270-281 (2014).
 23. W. Wang, L. Zhu, J. Qin, Y.-P. Chui, B. N. Li, and P.-A. Heng, "Multiscale geodesic active contours for ultrasound image segmentation using speckle reducing anisotropic diffusion," *Opt. Laser Eng.*, **54**, 105-116 (2014).
 24. J. Montel and A. Beghdadi, "A new interpretation and improvement of the nonlinear anisotropic diffusion for image enhancement," *IEEE T. Pattern Anal.*, **21**(9), 940-946 (1999).
 25. X. Qian, X. Jia, Z. Wang, B. Zhang, N. Xue, W. Sun, Q. He, and H. Wu, "Noise level estimation of BOTDA for optimal non-local means denoising," *Appl. Opt.*, **56**(16), 4727-4734 (2017).
 26. M. J. Black, G. Sapiro, D. H. Marimont, and D. Heeger, "Robust anisotropic diffusion," *IEEE T. Image Process.*, **7**(3), 421-432 (1998).
 27. L. J. Van Vliet, I. T. Young, and G. L. Beckers, "A nonlinear Laplace operator as edge detector in noisy images," *Comput. Vis. Graph. Image Processing*, **45**(2), 167-195 (1989).
 28. N. Kanopoulos, N. Vasanthavada, and R. L. Baker, "Design of an image edge detection filter using the Sobel operator," *IEEE J. Solid-st. Circ.*, **23**(2), 358-367 (1988).
 29. A. K. Azad, F. N. Khan, W. H. Alarashi, N. Guo, A. P. T. Lau, and C. Lu, "Temperature extraction in Brillouin optical time-domain analysis sensors using principal component analysis based pattern recognition," *Opt. Express*, **25**(14), 16534-16549 (2017).
 30. A. K. Azad, L. Wang, N. Guo, H.-Y. Tam, and C. Lu, "Signal processing using artificial neural network for BOTDA sensor system," *Opt. Express*, **24**(6), 6769-6782 (2016).
 31. M. A. Soto, G. Bolognini, and F. Di Pasquale, "Analysis of optical pulse coding in spontaneous Brillouin-based distributed temperature sensors," *Opt. Express*, **16**(23), 19097-19111 (2008).